Icarus 304 (2018) 143–161

Contents lists available at ScienceDirect

Icarus

journal homepage: www.elsevier.com/locate/icarus

Impact simulation in the gravity regime: Exploring the effects of parent body size and internal structure

P.G. Benavidez[a,b,*], D.D. Durda[c], B. Enke[c], A. Campo Bagatin[a,b], D.C. Richardson[d], E. Asphaug[e], W.F. Bottke[c]

[a] Departamento de Física, Ingeniería de Sistemas y Teoría de la Señal. P.O. Box 99, 03080 Alicante, Spain
[b] Instituto Universitario de Física Aplicad a la Ciencias y la Tecnología
[c] Southwest Research Institute, 1050 Walnut Street, Suite 300 Boulder, Colorado 80302 USA
[d] Department of Astronomy, University of Maryland, College Park MD, 20742 USA
[e] Arizona State University, Tempe, AZ

ARTICLE INFO

Article history:
Received 11 January 2017
Revised 19 April 2017
Accepted 31 May 2017
Available online 2 June 2017

Keyword:
Collisional physics
Impact process
Asteroid families

ABSTRACT

In this work we extend the systematic investigation of impact outcomes of 100-km-diameter targets started by Durda et al. (2007) and Benavidez et al. (2012) to targets of D = 400 km using the same range of impact conditions and two internal structures: monolithic and rubble-pile. We performed a new set of simulations in the gravity regime for targets of 400 km in diameter using these same internal structures. This provides a large set of 600 simulations performed in a systematic way that permits a thorough analysis of the impact outcomes and evaluation of the main features of the size frequency distribution due mostly to self-gravity. In addition, we use the impact outcomes to attempt to constrain the impact conditions of the asteroid belt where known asteroid families with a large expected parent body were formed. We have found fairly good matches for the Eunomia and Hygiea families. In addition, we identified a potential acceptable match to the Vesta family from a monolithic parent body of 468 km. The impact conditions of the best matches suggest that these families were formed in a dynamically excited belt. The results also suggest that the parent body of the Eunomia family could be a monolithic body of 382 km diameter, while the one for Hygiea could have a rubble-pile internal structure of 416 km diameter.

1. Introduction

Our understanding of the collisional evolution of populations of small bodies in the Solar System is based on knowledge of details of collisional physics, from the formation of impact craters to the destruction of the entire bodies. The key parameter traditionally used to study these impact outcomes is the specific impact energy, Q (kinetic energy of the projectile divided by the target mass). Studies of such fragmentation processes have given rise to what is commonly referred to as scaling laws. These consist of determining the critical specific energy (denoted by Q^*_D) required to disperse a target into a spectrum of individual and possibly reaccumulated objects, the largest one having half the mass of the original target. Consequently, Q^*_D is a function of target size, where two main regimes are identified: smaller bodies in the strength regime, where self-gravity is not important for holding the object together; and larger bodies in the gravity regime, where fragments can reaccumulate via the self-gravity of the components. The strength-scaling regime for small objects is mostly examined through laboratory impact experiments (e.g., Fujiwara et al., 1977, Arakawa 1999; also see Leliwa-Kopystyski and Arakawa 2014 for a review) while the impact outcomes of larger bodies are studied using numerical simulations.

In this latter case, Benz and Asphaug (1999) used a smoothed-particle hydrodynamics (SPH) method to simulate impacts into rocky and icy bodies in a large range of sizes. They found that gravity plays a dominant role in determining the outcome of collisions even involving relatively small targets. For example, in the size range considered in their work, from 3 cm to 100 km in radii, the enhanced role of gravity is not so much to prevent fracture prevention by gravitational compression, but rather to impede the escape of fragments due to their mutual gravitational attraction. Jutzi et al. (2010) performed simulations in the same size range as Benz and Asphaug (1999). Their results confirm that Q^*_D first decreases with target size in the strength regime (i.e., up to a few hundred meters in diameter) and then increases with target size

* Corresponding author: Departamento de Física, Ingeniería de Sistemas y Teoría de la Señal, Universidad de Alicante, P.O. Box 99, 03080 Alicante, Spain.
E-mail address: paula.benavidez@ua.es (P.G. Benavidez).

http://dx.doi.org/10.1016/j.icarus.2017.05.030
0019-1035/

in the gravity regime (see Asphaug et al., 2002; 2015; Jutzi et al., 2015 for reviews). In addition, they found that in the strength regime a porous body requires more energy to be disrupted than its non-porous counterpart while in the gravity regime the situation is reversed but the difference remains small.

The size spectrum of individual fragments produced in a catastrophic disruption is the so-called the size frequency distribution (SFD), usually expressed by a power law of the form $N(>D) \propto D^q$ (the cumulative representation). When this function is represented in a log-log plot we obtain a line with a slope of q, $q < 0$ such that there are more small bodies than big ones. The particular morphologies of SFDs have been used to characterize the impact outcomes of a range of targets. For example, in the case of a monolithic non-porous parent body, higher impact energies lead to a more continuous[1] fragment size distribution (Michel et al., 2003; Michel et al., 2004; Durda et al., 2007). Furthermore, Michel et al. (2003), considering pre-shattered non-porous targets with diameters of about 25 km, found that the SFD tends to be more continuous than those of monolithic non-porous targets (2). Durda et al. (2004) also investigated the efficiency of satellite formation during catastrophic disruptions. Subsequently, Durda et al. (2007) and Benavidez et al. (2012) analyzed, in a systematic way, the mean features resulting from impacts on both rubble-pile and monolithic parent bodies with diameters of 100 km. They showed that low-energy impacts into rubble-pile and monolithic targets produce different features in the resulting SFDs and that these are potentially diagnostic of the initial conditions for the impact and the internal structure of the parent bodies of asteroid families. In contrast, super-catastrophic events (i.e., high-energy impacts with large specific impact energy) result in SFDs that are similar to each other.

Many authors have used the fragment SFDs produced by various kinds of impact simulations to glean insights into parent body sizes and disruption conditions for asteroids families (e.g., Tanga et al., 1999, Durda et al., 2007; Benavidez et al., 2012). In particular, several authors have used the results of SPH codes to explore the disruption of $D > 100$-km-diameter parent bodies. Basically, what these studies do is to plot to the same scale the modeled SFD and the observed family SFD in a single chart. Modeled impacts assume a particular target size; therefore, the resulting largest remnant and SFD of associated fragments may need to be offset in size to the left or right to match the observed SFD. This offset suggests a larger or smaller parent body for the observed family. However, in some cases, especially when the parent body is actually quite different in size from the particular modeled target (usually 100-km-diameter), the methodology used to date could provide results that are not entirely accurate. Specifically, the SFDs of $D >>$ 100-km-diameter targets could have significantly different features compared to those for a $D = 100$ km target, i.e., relative mass of the largest fragment and/or the SFD slope of smaller fragments. This is because the effects of gravity in the reaccumulation process of such larger bodies do not simply scale linearly. It is worth mentioning that such an approach to match the SFD is the lowest-order approximation; it is merely a first approximation for estimating the parent body size for an observed family. Ideally, one would use this technique to then run another matrix of simulations using a suite of parent-body targets with diameters around that predicted from the SFD 'shift' approximation, like the Karin family simulations of Nesvorný et al. (2006).

The asteroid belt in general, and asteroid families in particular, provides an outstanding natural laboratory for exploring the outcomes of collisional events in a wide range of sizes. These populations allow us to study both the collisional formation process of the Solar System and its subsequent evolution over time. However some numerical models of the collisional evolution of main-belt asteroids, which use as input the impact outcomes mentioned in the previous paragraph, can have difficulty reproducing the observed SFDs of asteroid families. For example, Cibulkova et al. (2014) propose a new six-part collisional model of the asteroid belt. Relying on the collisional origin of asteroids families, this study assessed whether the number of synthetic asteroid families created during the simulation agrees with the number of observed families. Then, they considered to two models: monolithic and rubble-pile asteroids, concluding that monolithic asteroids are in best agreement with the observations compared to the rubble-pile counterpart. However they do not discard the possibility that some part of the asteroid population could be consistent with rubble-pile structures. There are many possible reasons for this – family members lost to resonances, collisional evolution, interlopers in the family, and so on. Here we focus on one particular issue, namely whether the fragment SFDs made by the disruption of $D = 100$-km-diameter parent bodies are a good match to the fragment SFDs made when larger worlds break up ($D = 400$ km). On the other hand, another issue where SPH/N-body impact outcome became useful is constraining the amount of mass hidden below our current detection limits (Bottke et al., 2005). In order to do this it is necessary to compare the observed families to the scaled impact outcomes, following the procedure explained in the previous paragraph. These examples highlight the need to extend SPH simulations to larger targets, in order to test the known scaling laws for larger targets and characterize the resulting SFDs for different impact conditions.

While the existence of monolithic large bodies (about $D = 400$ km) is broadly accepted, the existence of rubble-pile bodies of such size is controversial. However, we allow the possibility in the present study. On the other hand, Durham et al. (2005) considered ice bodies and found that ~1000 km ice bodies (if cold) can have some residual porosity at pressures of 100 MPa, typical of asteroid cores. Theory and observation indicate that everything bigger than a few 100 km in diameter would have melted if formed in the inner solar system in the first few Ma, so a 400-km-diameter rubble-pile would have to be a second-generation object, or else something that accreted after a few Ma (e.g., far from the Sun). The study by Campo Bagatin et al. (2001) on the abundance of rubble-piles in the main belt found that -under specific conditions- the presence of rubble-piles up to 500 km diameter cannot be ruled out.

Based on the evidence mentioned in the preceding paragraphs, we have decided to extend the systematic investigation of impact outcomes started by Durda et al. (2007) and Benavidez et al. (2012) to 400-km-diameter targets using the same range of impact conditions and two internal structures: monolithic and rubble-pile. In Section 2 we briefly recall the numerical method used to perform the simulations. In Section 3 the results of the comparison between our systematic numerical investigations of rubble-pile versus monolithic targets are presented. In Section 4 a comparison between results from our numerical models and observed asteroid families is discussed. Finally, in Section 5, we present our conclusions.

2. Method

In this work we performed a series of simulations with the same numerical technique used in our previous impact simulation studies (Durda et al., 2004; Benavidez et al., 2012), which is essentially the same numerical scheme introduced by Michel et al. (2001, 2002) to study the formation of asteroid families. As this technique is widely accepted and fully described in the mentioned

[1] This term is used by Michel et al. (2003) to mean that the SFD contains intermediate-sized bodies.

articles we just summarize here only the main features and refer the reader to Durda et al. (2004) and Benavidez et al. (2012) for further details.

The technique includes both a Smoothed-Particle Hydrodynamic (SPH) code, which models the pressures, temperatures, and energies of asteroid–asteroid impacts, and an efficient *N*-body code, which computes the dynamics under the mutual gravitational interactions of hundreds of thousands of individual collision fragments in an expedient manner.

Initially, the 3D SPH code (Benz and Asphaug 1994, 1995) is used to model the actual impact. This deals with the collision phase of any catastrophic impact between two asteroids. Gravitational self-compression of the target during the impact phase is treated as an overburden stress that must be exceeded before fracture can initiate (Asphaug and Melosh, 1993). A Tillotson equation of state model (Tillotson, 1962) for basalt is used to relate the pressure to density and internal energy. This model provides excellent results when compared with ejecta velocities derived from laboratory impact experiments.

When the impact phase of the simulations is sufficiently complete (crater formation/ejecta flow fields established with no further fragmentation/damage), the outcome of the SPH model is handed off as the initial conditions for the *N*-body simulation phase. To track the trajectories of collision fragments we use the cosmological *N*-body code `pkdgrav` (Stadel, 2001), modified as described in Richardson et al. (2000) (see also Leinhardt et al., 2000; Leinhardt and Richardson, 2002). The tree component of the code provides a convenient means of consolidating forces exerted by distant particles, reducing the computational cost. The parallel component divides the work evenly among available processors, adjusting the load at each time-step according to the amount of work done in the previous force calculation. The *N*-body simulations are run, with time steps equal to 10^{-5} in units of year/2π (e.g., ~50 s), to a time of about 17.5 days (i.e., 30,000 time steps) after the impact. Our choice of 17.5 days of *N*-body simulation time after impact was set by a combination of available CPU resources and because the number of satellites and satellite systems that one would expect to see due to formation and dissolution of transient binaries should not change significantly after that time for the impact conditions that we are modeling. That time is on the order of the dynamical time for an object dispersed to its Hill sphere at typical asteroid distances, which should be a rough upper limit for most of the evolution to reach equilibrium in this scenario.

2.1. Target internal structures and impact conditions

For the present study, impact outcomes of 100-km- and 400-km-diameter targets made of different internal structures (monolithic and rubble-pile) are compared. Since previous studies used 100-km-diameter targets, for the current study we only performed new simulations with 400-km-diameter targets. Specifically, we simulated impacts between a monolithic impactor and both monolithic and rubble-pile targets of $D = 400$ km. For the present work we do not consider targets with other sizes. The following describes how each target is built and the impact condition considered.

We construct rubble-pile targets[2] (see Asphaug et al., 2002) by filling the interior of a spherical shell (the target envelope, with $D = 400$ km) with solid basalt spheres having a distribution of diameters between 30 km and 80 km. We then decrease the density and strength of SPH particles in the contact zones between the solid components from 2.7 to 1.3 g/cm^3 as a way to represent the damage inside the target. The remainder of the target body is void space, setting the bulk density of the target equal to 1.835 g/cm^3 (corresponding to a target mass of 6.15×10^{19} kg). Resolution is of concern, and to ensure physical modeling we require at least 5 SPH particles across the smallest rubble-pile spheres of the target, to capture the shock wave. This results in the lower boundary for the diameter of the basalt spheres stated above (30 km). In contrast, the monolithic target is assumed to be spherical and is composed of solid basalt with a density of 2.7 g/cm^3 (corresponding to a target mass of 9.05×10^{19} kg). For a comprehensive analysis of the impact outcomes we also used our previous simulations for targets of 100 km diameter which are made in a similar way than the ones described above, yielding a target mass of 1.414×10^{18} kg and 9.60×10^{17} kg for monolithic and rubble-pile internal structures respectively. The resolution of both monolithic and rubble-pile targets is the same, 100,000 particles packed into an initial 100-km or 400-km-diameter sphere. Comparable particle diameters (with fewer particles) were used for the impactor.

Here we used the same matrix of impact conditions explored in Benavidez et al. (2012) and Durda et al. (2004). Thus, we have a large set of impact simulations for two different sizes ($D = 100$ and $D = 400$ km) and different internal structures. These simulations comprise a homogenous set of 600 simulations covering a wide range of impact speeds (from 3 to 7 km/s), impact angles (from 15° to 75° with 15° increments) and impactor diameters. The average speed of the velocity distribution of the asteroid population is about 5 km/s, with a significant tail toward higher speeds (Dell' Oro and Paolicchi, 1998). However in the present study, we have focused on the range of 3 to 7 km/s to maintain uniformity with simulated conditions in previous studies. Taking into account that target mass changes for different target sizes, we chose the logarithm of the target-to-impactor mass ratio as an indicator of the impactor size. This ratio behaves as a standard parameter to compare simulations with the same specific impact energy. Therefore, the impactor diameters correspond to 3.0, 2.6, 2.2, 1.8 1.4 and 1.0 in terms of the logarithm target-to-impactor mass ratio, which correspond to an impactor size between ~10 to ~46 km for a 100-km-diameter target and to a size range between ~40 and ~186 km for 400-km-diameter target.

3. Results

In this section we present the results obtained for our full set of simulations. The outcomes of the impact simulations range from cratering events to super-catastrophic disruption events. In the following, we analyze the impact outcomes in terms of the specific impact energy, the critical specific impact energy and its relationship with the impact angle, and the resulting modeled SFDs.

3.1. Specific impact energy

Fig. 1 shows the largest remnant mass ratio (M_{LF}/M_T) versus specific impact energy for our SPH/*N*-body simulations considering rubble-piles and monolithic targets of $D = 100$ km and $D = 400$ km. In each plot the dashed line indicates the limit of a catastrophic disruption ($M_{LF}/M_T = 0.5$). All the results above the line correspond to cratering events while those below the line are catastrophic impacts. As expected, the larger the impactor the more catastrophic the event is, due to impact energy increase. Fig. 1 also shows that for analogous impact conditions, the relative mass of the largest fragment is greater in the case of a $D = 400$-km target compared to $D = 100$-km target, for most cases. This is true for both types of internal structures studied, indicating that self-gravity is more important for large targets. This trend is not surprising, but as we show in Section 3.4, it determines certain features in the SFD produced in a given impact.

[2] The number of particles in the target is constrained by computational resources. In a future study it would be needed to assess the detailed effect of resolution.

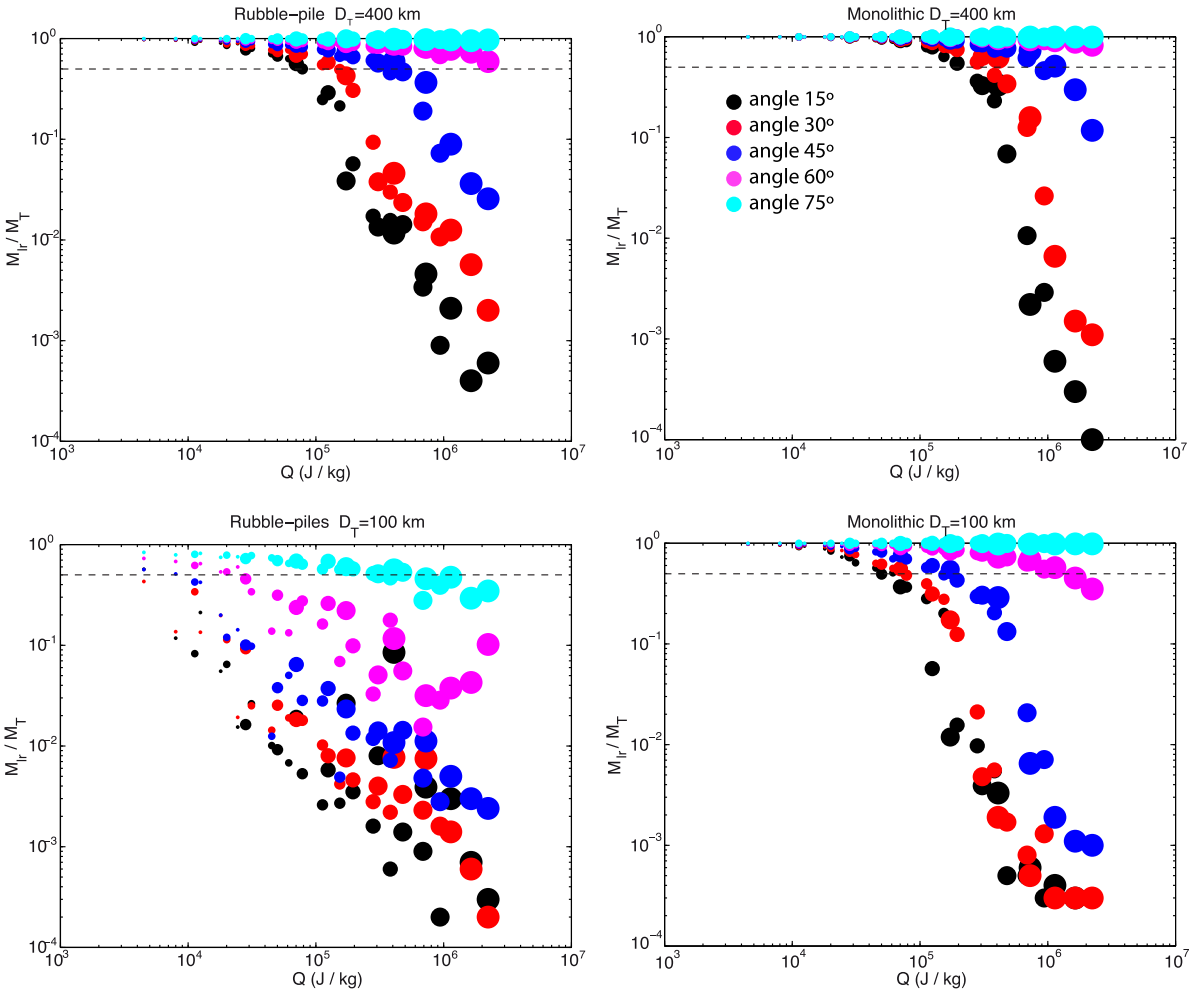

Fig. 1. Largest remnant mass ratio versus specific impact energy for our SPH/*N*-body simulations for rubble-pile and monolithic targets with diameters of 100 and 400 km, as indicated by legend above each box. Dot sizes are coded according to impactor diameter, where smaller dots represent smaller impactors. The dashed line indicates the catastrophic disruption ($M_{LF}/M_T = 0.5$) threshold. The colors indicate impact angle (see legend in top-right box).

Concerning rubble-pile impact outcomes, significant differences from those for solid, monolithic targets can be seen in Fig. 1 (left column). At low specific impact energy, rubble-pile targets of $D = 100$ km are most vulnerable to catastrophic collisions even at quite oblique impact angles.[3] In contrast, impacts onto targets of $D = 400$ km at the same specific impact energy result in $M_{LF}/M_T > 0.5$ indicating cratering events with most of the fragmented material either reaccumulated or retained during the collision. Therefore in impacts onto $D = 100$ km targets with the same impact conditions, gravity is less important in a relative sense, leaving a more disruptive outcome. At higher specific impact energies (over 10^5 J/kg) most impact events onto $D = 400$ km targets with impact angles smaller than 60° produce catastrophic disruption.

3.2. Critical specific impact energy

In this section we compare the Jutzi et al. (2010) scaling law with our results (where possible). Usually the scaling parameter is defined in terms of the critical specific impact energy (Q^*_D), which results in the escape of half of the target's mass. Normally it is assumed to follow a power law of the form:

$$Q^*_D = Q_0\left(\frac{R_T}{1\text{cm}}\right)^a + B\rho\left(\frac{R_T}{1\text{cm}}\right)^b,$$

where R_T is the radius of the target, ρ its density in g/cm^3 and Q_0, B, a, and b are constants to be determined.

Jutzi et al. performed simulations of porous ($\rho = 1.3$ g/cm^3) and non-porous ($\rho = 2.7$ g/cm^3) targets impacted at 3 and 5 km/s and impact angle 45° with different projectile sizes. From these simulations they fit a scaling law to their data. In an attempt to compare our results with this previous study we selected the comparable cases from our simulations and calculated Q^*_D for them. Among our set of simulations the only comparable cases are the monolithic ones, given that the structure of the targets is similar and the assumed density is the same.

We are thus limited to monolithic cases with impact speed of 5 km/s and impact angle of 45°. Note that as we did not determine Q^*_D precisely we considered a narrow range close to $M_{LF}/M_T = 0.5$ between 0.43 and 0.63 as the best approach to estimate it. For those cases with impact speed of 3 km/s, we did not get results that satisfy this condition for the $D = 400$ km target. Unfortunately, our rubble-pile runs are not directly comparable to the Jutzi et al. porous runs because of the different densities and particularly because of the manner in which we handle target porosity.

Fig. 2 represents the fit of the scaling law estimated by Jutzi et al. and our two comparable cases (monolithic targets of

[3] This particular set of simulations (rubble-pile target of 100 km) was previously analyzed in Benavidez et al. (2012). So here we refer to them only in the context of the whole set of simulations.

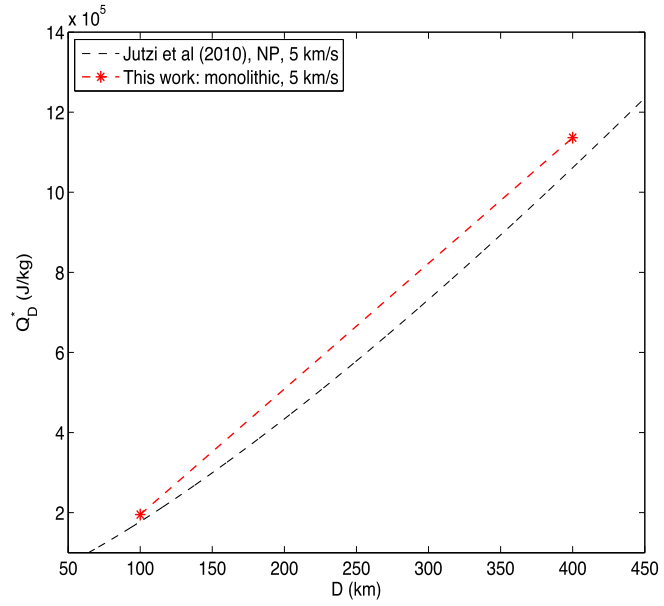

Fig. 2. (a) Critical specific impact energy (Q^*_D) as function of target diameter. The black dashed line represents the Jutzi et al. (2010) fit for non-porous (NP) (basalt material), impact speed 5 km/s and 45° impact angle. Red asterisks are our result for a monolithic target impacted under the same impact conditions. (For interpretation of the references to colour in this figure legend, the reader is referred to the web version of this article.)

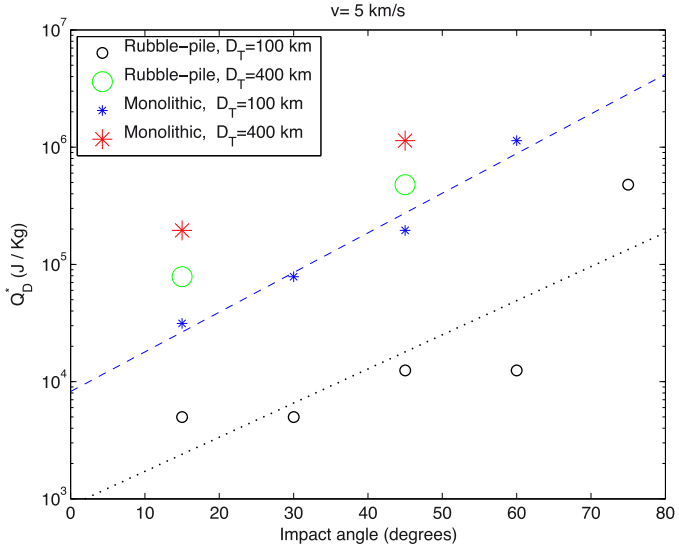

Fig. 3. Critical specific impact energy (Q^*_D) as function of impact angle for impact speed of 5 km/s. Dot sizes are coded according to target diameter, with small symbols representing the target of $D = 100$ km and the large symbols corresponding to $D = 400$ km targets. Dotted lines show the best exponential fit for monolithic and rubble-pile $D = 100$ km targets. (For interpretation of the references to colour in this figure legend, the reader is referred to the web version of this article.)

$D = 100$ km and $D = 400$ km with impact events at 5 km/s at 45°). We find our $D = 100$ km case lies on the scaling law, while the $D = 400$ km case is slightly above the line (note the linear scale). This small difference could either be a statistical effect or an actual trend to a steeper slope for larger targets. More simulations are needed to confirm this, and would deserve further deeper studies.

3.3. Critical specific impact energy vs. impact angle

Fig. 3 shows the critical specific impact energy as a function of impact angle at an impact speed of 5 km/s, for rubble-pile and monolithic targets with $D = 100$ and $D = 400$ km. We do not have Q^*_D for all 20 cases because we did not choose impact conditions to bracket Q^*_D specifically. However, the 13 cases for which we could calculate Q^*_D allow us to observe that as the impact angle becomes more oblique, the critical specific energy required for disruption increases. As Leinhardt and Stewart, (2012) pointed out this issue is due to the impact parameter ($b = (R_T + r_p) \sin\theta$, θ being the impact angle while R_T and r_p are the target and projectile radii) increasing with the impact angle. Jutzi et al. (2010) and Benz and Asphaug (1999) also mentioned this trend but did not quantify its behavior. Pierazzo and Melosh (2000) observed different kinds of dependences for the shock pressure, temperature and energy of the target and projectile with $\sin\theta$. Their results indicate that only the vertical component of the impact velocity plays a role in an impact.

From our results presented in Fig. 3 it is evident that there is a relation between Q^*_D and the impact angle. However the Q^*_D values for impact angles from 15° to 60° are fairly similar but those for 75° differ by more than an order of magnitude from those for smaller angles. This only happens for the $D = 100$ km rubble pile, because this is the only target for which we have Q^*_D for 75°. For other targets we should run some extra cases with a larger projectile. It is therefore difficult to discern whether these are two linear relationships intersecting somewhere between 60° and 75° or an exponential relationship. We fit an exponential function ($Q^*_D = a\, e^{b\theta}$), where a and b are constants to be determined. The best fit for monolithic and rubble-pile targets of $D = 100$ km is represented in logarithmic scale for Q^*_D in the figure. We did not try to fit the $D = 400$ km target because too few points (only two) are available. The fit for the monolithic target gives $a = 8221$ and $b = 0.078$ with a correlation coefficient of 0.969, while for the rubble-pile $a = 876$, $b = 0.067$ with a correlation coefficient of 0.705. The high Q^*_D value for the oblique impact angle of 75° mentioned above is the reason why the fit gets worse. Further studies including impacts between 60° and 75° could help to determine a more robust dependence.

3.4. Cumulative size frequency distributions

In this section we analyze the cumulative SFDs resulting from our impact simulations. Henceforth, when referring to the SFD we will be describing the cumulative size-frequency distribution (as opposed to the differential size-frequency distribution). First we describe the main features of the SFDs in a more qualitative manner and then we parameterize and quantify the SFDs in more detail.

3.4.1. Qualitative analysis

Fig. 4 shows the main features of the SFD morphologies, which we will use for reference. The overall features of the SFDs observed are reviewed in this section, but the SFDs for different impact angles are shown in Appendix A.

A common feature of the resulting SFDs for 400-km targets is that their morphology appears rather similar to a “hockey stick” (see Fig. 4a), which is typical for a cratering event, but also moderate fragmentation, when limited mass is lost from the primary. Super-catastrophic impacts at 6 and 7 km/s and impact angle $\leq 45°$ are the exception, where the SFD changes from a single power law at impact angle of 15° to a “convex” curve for 45° (see Fig. 4b). By “hockey stick” morphology we mean that it is possible to distinguish two parts in the modeled SFDs: at larger fragment sizes the ‘blade’, which is related to the size ratio between the two largest fragments (D_1/D_2, with D_1 equal to the largest fragment (or remnant) diameter and D_2, the second largest), and for smaller fragment sizes the ‘shaft’, which is well fitted by a single power law. The contrast between the length of the ‘blade’ and the slope of the ‘shaft’ in the SFDs for targets of $D = 100$ km compared to ones of

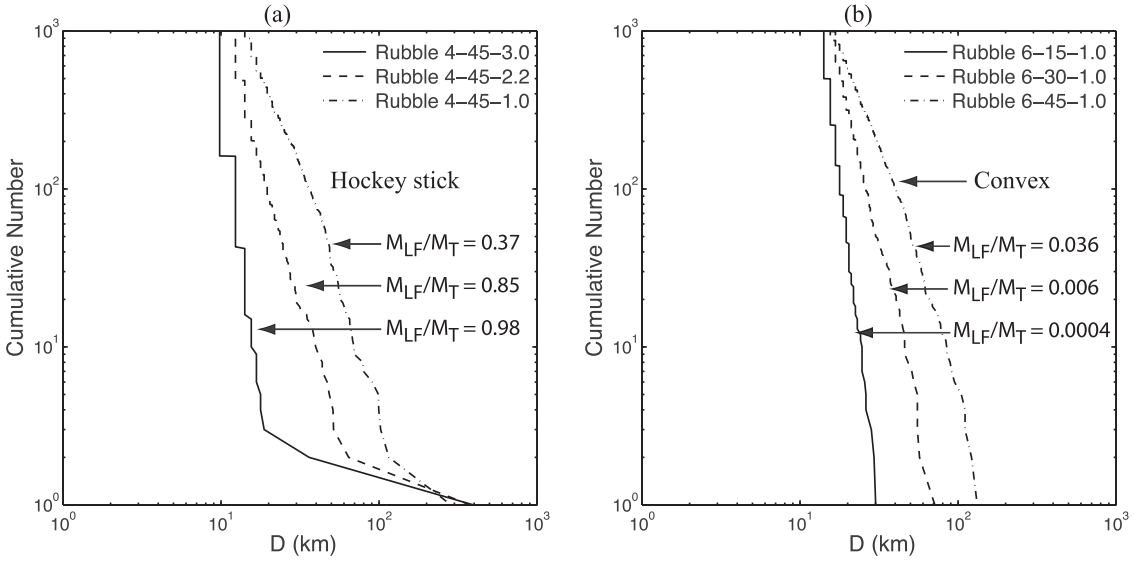

Fig. 4. (a) Change in the SFD morphology when the impactor size increases (at moderate impact energy). The plotted cases correspond to a rubble-pile D= 400 km target at impact speed 4 km/s and 45° impact angle. The largest remnant mass ratio (M_{LF}/M_T) indicates the fragmentation level. (b) Change in the SFD morphology for super-catastrophic events for increasing impact angles (at high impact energy). The plotted cases correspond to a rubble-pile D= 400 km target at impact speed 6 km/s and the largest projectile simulated (~186 km).

D= 400 km makes it very difficult to match both features for the same impact conditions.

3.4.2. Quantitative analysis

Fig. 5 shows the SFD slope as a function of the impact energy (Q). Two types of symbols were used to distinguish between cratering (filled circles) and catastrophic impacts (open circles). Although some points overlap, a slight trend is observed for D = 400 km targets (monolithic and rubble-pile) and the D = 100 km monolithic target. There is a tendency to shallower slope for increasing impact energy in the cratering regime. However, when the critical fragmentation energy is reached, the slope of the SFDs becomes steeper as the impact energy increases. On the other hand, the SFD slope of smaller fragments for D = 100 km rubble-pile targets impacted at $\leq$ 45° start shallow (in the range of −4 to −2) for low impact energies, and turn steeper as the impact energy increases, due to in this case most impact conditions resulting in breakup of the target. However the cases for more oblique angles remain with a shallower slope.

Figs. 6 and 7 show the mass ratio of the second-largest fragment (denoted by M_2/M_T) as a function of the impact energy. In these figures it is easier to see the transition from the cratering to the catastrophic regime mentioned above. It is also interesting to note that M_2/M_T follows a strong linear trend (in a log-log plot) with specific impact energy. It has a positive slope in the cratering regime and turns to negative slope for fragmentation events, with decreasing M_2 as the impact energy increases. It is worth mentioning that this trend is followed by both monolithic and rubble-pile targets of D= 100 km and 400 km for each impact angle. Although for more oblique impact angles cratering events dominate the trend and there is more dispersion in the results, especially for larger projectiles.

3.5. Ruling out/constraining the shift factor

The approach normally applied for comparing the SFDs allows us to achieve two goals: to estimate the impact conditions that most closely match the observed family SFD (morphologically), and to calculate the size of its parent body. This approach consists of plotting together at the same scale both the modeled and the actual family's SFDs. Since it is easy to estimate the shift factor,[4] the modeled distribution needs to be offset in size to match the observed SFD. The magnitude of this offset in logarithmic units yields the factor needed to increase or decrease the diameter of the actual family parent body from the 100-km-diameter parent body of the modeled family (Durda et al., 2007 and Benavidez et al., 2012).

The described method should be applied with some caution due to the fact, as we warned in the introduction and as discussed in Durda et al. (2007) and Benavidez et al. (2012), that this strategy assumes that impact outcomes scale linearly with the target size. As we discussed in Section 3.4 the modeled SFD undergoes significant changes when we move from a D = 100 km to a D = 400 km target that are not easily matched by a single offset of the scaled SFD. We also performed some extra simulations for 350 and 450 km rubble-pile targets because we are focused on the range of large bodies where self-gravity is important. To verify the validity of this approach, we performed the following test. Assuming that the outcome for a 350 km target corresponds to a given 'true family' we compared its SFD to the modeled ones for 400 and 450 km targets and estimated the magnitude of the shift factor, the estimated parent body diameter and its relative error.

We selected four cases covering a range from low to high impact energy for rubble-pile targets. Table 1 lists the selected cases, impact conditions, largest remnant mass ratios, size ratios of the largest- and second-largest fragments, estimated slope and largest fragment diameter. Furthermore, the estimated shift factor and expected parent body diameter corresponding to the match to the SFDs' shape for 400 and 450 km targets are listed with the relative error for the latter. We observe that when impact energy is low or moderate (e.g., first three cases), the error in estimating the parent body diameter increases to about 5% (less than 20 km in size) when we try to fit the impact outcome of a 350 km target with a 450 km target. Conversely, for high impact energy, which produces super-catastrophic impacts, the error increases to almost 17%, which is about 60 km in size.

[4] The shift factor is estimated as the ratio between the diameter of the largest member of a family and the diameter of the largest fragment from a given simulation that best matches the SFD.

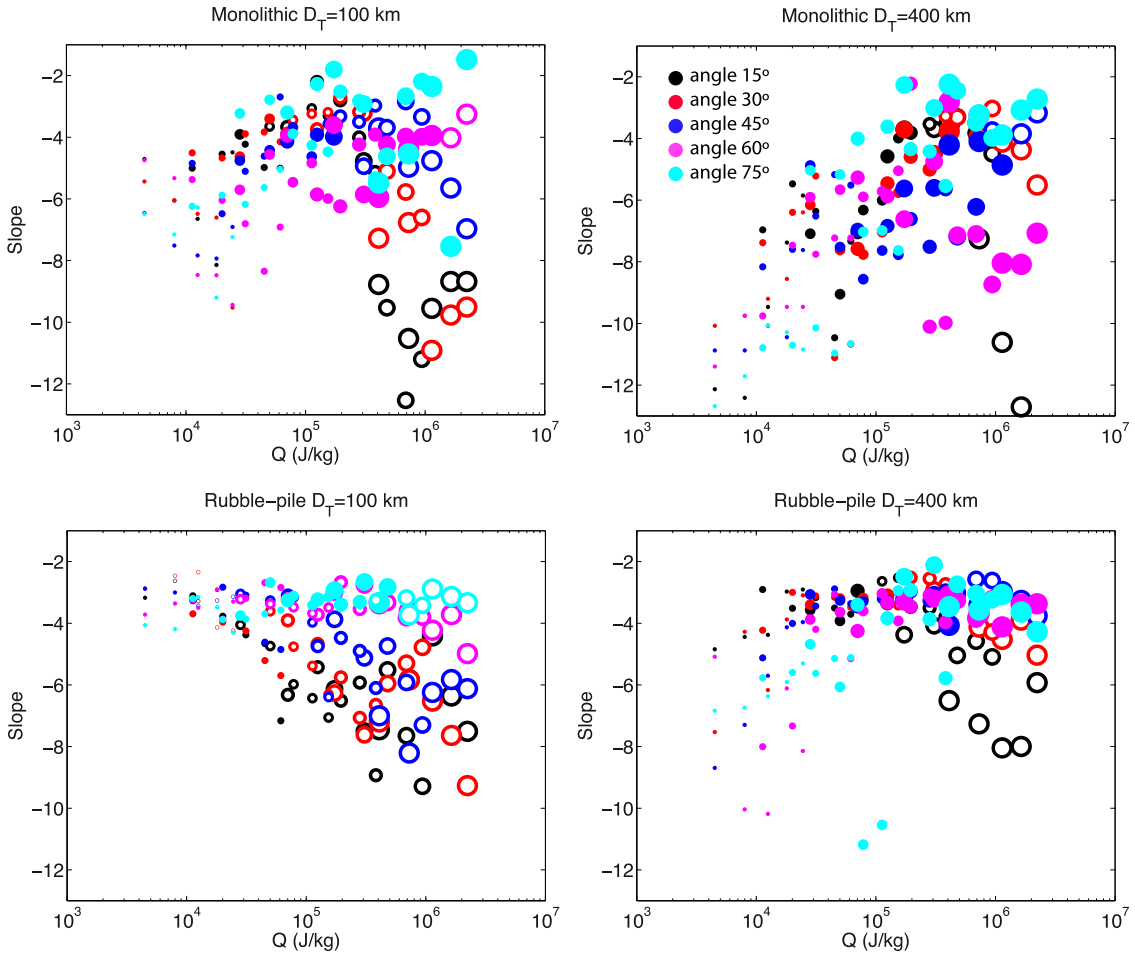

Fig. 5. SFD slope as a function of the specific impact energy (Q). Dot sizes are coded according to impactor diameter. Filled circles indicate cratering events and open circles catastrophic events.

Table 1
Input parameters and results from some extra runs.

D_T (km)	$^{v}(\frac{km}{s})$	Impact angle(°)	$^{Log}(\frac{M_T}{m_{imp}})$	$^{Q}(\frac{J}{kg})$	$(\frac{M_{LF}}{M_T})$	$(\frac{D_1}{D_2})$	Slope	D_1 (km)	[a]Shift factor	[b]D_{pb} (km)	[c]E_r (%)
350	4	30	2.2	5.02×10^4	0.69	4.98	−3.59	309			
400	4	30	2.2	5.02×10^4	0.74	4.16	−3.20	362	0.85	341	2.5
450	4	30	2.2	5.02×10^4	0.81	7.24	−3.50	420	0.74	331	5.4
350	6	15	2.6	4.51×10^4	0.65	4.10	−3.29	304			
400	6	15	2.6	4.51×10^4	0.71	5.17	−3.50	356	0.85	342	2.3
450	6	15	2.6	4.51×10^4	0.75	5.42	−3.64	408	0.75	338	3.4
350	5	45	1.8	1.95×10^5	0.65	4.15	−3.19	304			
400	5	45	1.8	1.95×10^5	0.66	4.27	−2.97	347	0.88	350	0.12
450	5	45	1.8	1.95×10^5	0.76	6.29	−3.79	410	0.74	334	4.6
350	7	45	1.0	2.23×10^6	0.02	1.13	−3.83	86			
400	7	45	1.0	2.23×10^6	0.03	1.26	−3.76	118	0.73	292	16.6
450	7	45	1.0	2.23×10^6	0.02	1.02	−2.99	126	0.68	306	12.6

[a] Shift Factor to 400 km=D_1(for D_T = 350 km)/D_1(for D_T = 400 km)
[b] Estimated parent body diameter, D_{pb} (from a 400 km target)= shift factor × 400
[c] Relative error, E_r= |350-D_{pb}| × 100/350

4. Modeled families' SFDs revisited

In this section we revisit the investigation of asteroid family formation by impact events started by Durda et al. (2007) and extended by Benavidez et al. (2012). Specifically, we determine if any asteroid family matches the features seen in the modeled SFDs. Taking into account that the shift factor should be constrained, we limited this investigation to families with large expected parent bodies. The procedure applied to determine families is detailed in Nesvorný et al. (2005). Some of the families analyzed are suspected to have interlopers among their larger members, which can affect the shape of the observed family SFDs. When possible, such interlopers have been removed from the SFD before comparison with the modeled SFDs (see Table 1 in Durda et al. (2007) for more detail about interlopers).

As a starting point, we select asteroid families with an alternative estimation of the parent body size with respect to previous estimations of its size by methods other than SPH/*N*-body simulations, following the approaches described by Tanga et al. (1999) and Campo Bagatin and Petit (2001). The former introduces

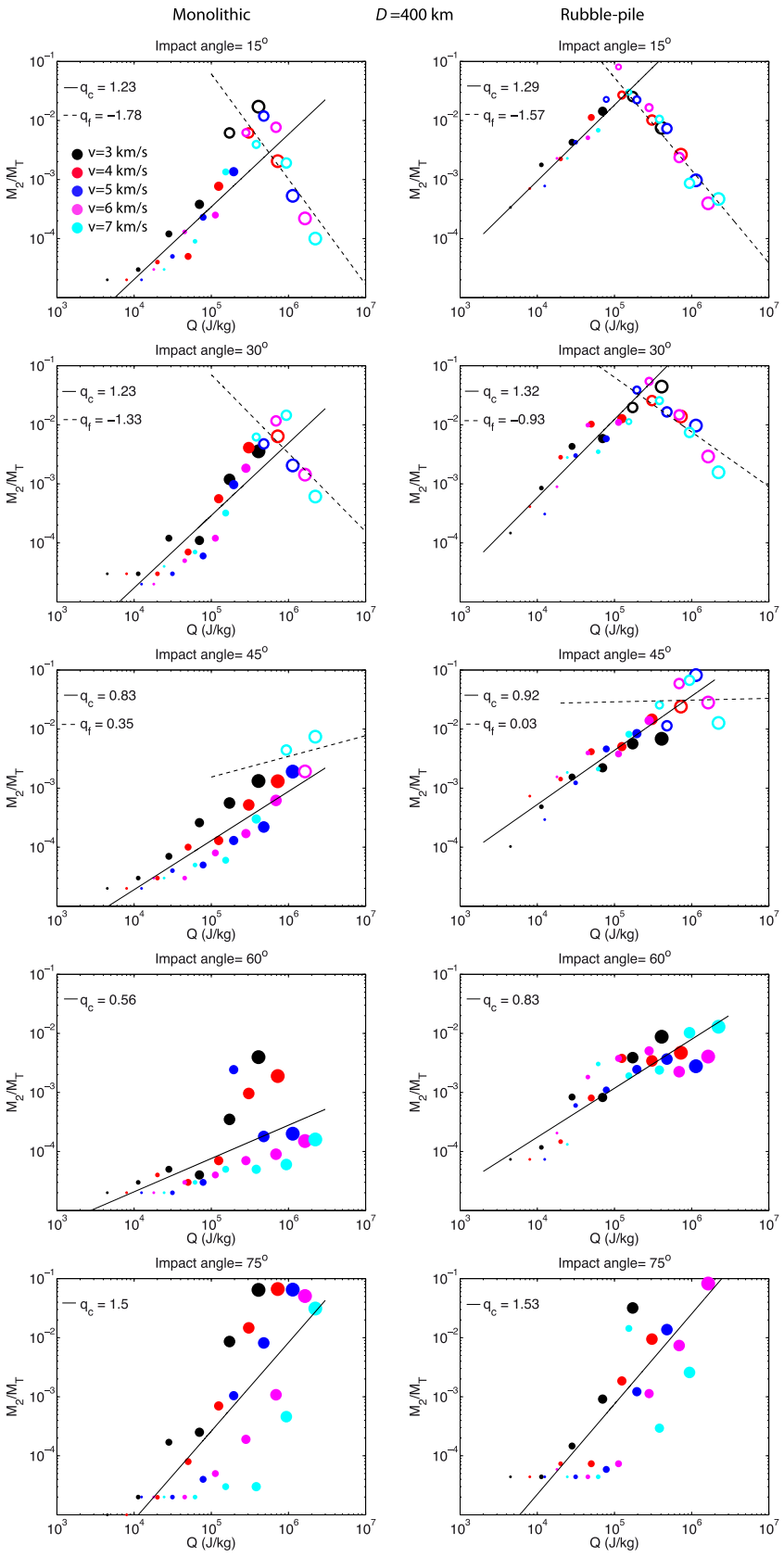

Fig. 6. Mass ratio of the second-largest fragment (denoted by M_2/M_T) as a function of the impact energy for monolithic and rubble-pile targets of $D = 400$ km. Dot sizes are coded according to impactor diameter. Filled circles indicate cratering events and open circles catastrophic events. Where possible, the fit to the data of each regime is shown and the slope is indicated in each box as q_c and q_f respectively. Colors indicate impact speed. Note that the fit for 45° impact angle might not be reliable as appear to be entering a regime where that behavior is changing.

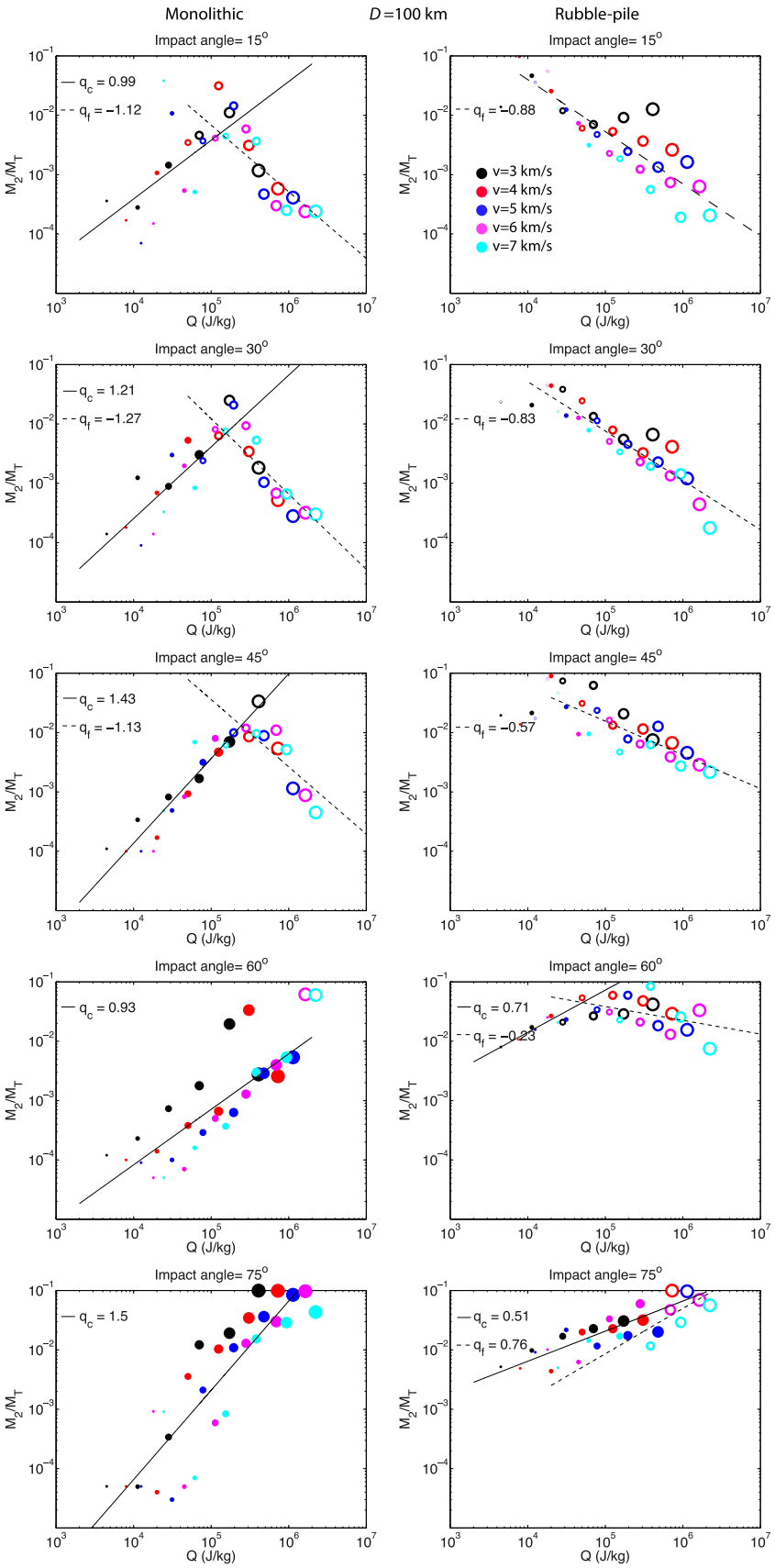

Fig. 7. Mass ratio of the second-largest fragment (denoted by M_2/M_T) as a function of the impact energy for monolithic and rubble-pile targets of $D = 100$ km. Dot sizes are coded according to impactor diameter. Filled circles indicate cratering events and open circles catastrophic events. Where possible, the fit to the data of each regime is shown and the slope is indicated in each box as q_c and q_f respectively. Colors indicate impact speed.

Table 2
Investigated families with large parent body.

Family	Tanga et al. (1999)		Campo Bagatin and Petit (2001)		Spoto et al. (2015)	
	D_{pb} (km)	$(\frac{M_{LF}}{M_{PB}})$	D_{pb}(km)	$(\frac{M_{LF}}{M_{PB}})$	Age (Myr)	
					IN side	OUT side
Hygiea	481	0.61	513	0.5	1330 ± 300	1368 ± 329
Vesta	468	0.95	468	0.99	930 ± 217	1906 ± 659
Themis	369	0.31	460	0.2	2447 ± 836	3782 ± 958
Eunomia	284	0.73	–	–	1955 ± 421	1144 ± 236

Table 3
Impact conditions that best match the observed families.

Family	Impact condition[a]	$(\frac{M_{LF}}{M_{PB}})$	Shift factor	D_{pb} (km)	χ^2
Eunomia	M 6–45–1.0	0.3	0.95	382	36
Hygiea	R 7–60–2.6	0.94	1.04	416	7
Vesta	M 6–75–1.8	0.99	1.17	468	1
Themis	Not good fit				

[a] The first letter(s) indicates the internal structure of the target (R for rubble-pile and M for monolithic); the numbers indicate impact speed-impact angle-log(M_T/m_p).

an approach for modeling the SFD from catastrophic impacts based on very simple geometric considerations. This approach assumes that fragments have convex shapes and takes into account only geometric constraints imposed by the finite volume of the parent body and the fact that fragments should not overlap with each other. An improvement to this model was presented by Campo Bagatin and Petit (2001). The main feature of the new approach is that they simulated the largest remnant and how fragments are formed in a more realistic way, considering the possibility of changing the shape of the largest remnant and the mass ratio between the largest fragment and target body. Then, from the subset of families selected by these authors we chose the families with large expected parent bodies (of order $D = 400$ km) to compare with our new set of simulations. This procedure ensures the shift is appropriately small, so we have higher confidence when matching the SFDs.

Table 2 lists the chosen families, the parent body diameter (D_{pb}), the largest fragment mass ratio estimated by the two approaches and the age estimated recently by Spoto et al. (2015). They used a least square fit to the V-shape in the (proper a-1/D) plane that asteroid leave after a breakup. Then, they have two age estimations, one for the low proper a (denoted as IN side) and the other for the high proper a (denoted by OUT side). We investigated four asteroid families: Hygiea, Vesta, Themis and Eunomia. To measure a match between our simulation and the observed families we calculate the chi-square (χ^2) to find the best matches for both monolithic and rubble-pile targets. In order to calculate χ^2, only fragments larger than $D > 17$ km were considered. It was done to avoid including the part of the resulting SFD where the stair effect become apparent because the code resolution limit is close. In the following, we present the results for each asteroid family.

Figs. 8 and 9 show the best matches, it is said those with lower χ^2. We did not find a statistically significant global minimum, so we consider χ^2 values for these runs to be statistically equivalent. Then, we plotted those cases with χ^2 up to twice the minimum χ^2 value. The results of the present study are listed in Table 3, namely the impact conditions the best match the family SFD, the largest fragment mass ratio corresponding to such impact conditions, the shift factor, the estimated parent body diameter and the estimated χ^2 value. Since χ^2 value is statistically equivalent for the cases shown in these figures, we selected from among of them those that best match visually the family SFD, mainly at the end of larger fragments, to be included in Table 3.

4.1. Eunomia family

The Eunomia family is the largest family in the central main belt, with 2772 members and a largest fragment diameter of 255 km. Spectroscopic analysis of the family from Mothé-Diniz et al. (2005) combined with previous data suggest some surface inhomogeneities or the action of space weathering. Mothé-Diniz et al. also propose that the presence of T- and X-class asteroids, classes compatible with iron meteorites, suggests the possibility that the formation of the Eunomia family may have been the result of the catastrophic breakup of a differentiated body. However, they also claim that they cannot rule out if these objects are interlopers.

Fig. 8 (upper panels) shows the best matches to the Eunomia family for $D = 400$ km monolithic and rubble-pile targets. We identified three different impact conditions with a monolithic target that produce SFDs quite similar to the one observed for this family (Fig. 8a). The best match (case M 6-45-1.0) is an impact at 6 km/s with a projectile of ~186-km-diameter and an impact angle of 45°. This is an event with high impact energy that produces a super-catastrophic disruption with a largest fragment mass ratio of 0.3. The parent body diameter estimated from these impact conditions is 382 km, which is about 100 km larger than predicted by the geometric approach of Tanga et al. (1999).

For completeness, Fig. 8b shows the "best" rubble-pile matches. The minimum values of χ^2 shed cases with the second largest fragment fairly larger than the observed in Eunomia. It is also interesting that –allowing a $\chi^2 = 4.5$ $\chi^2_{\min}$– at least four different impact conditions match the observed SFD for fragments larger than ~25 km (dotted lines in Fig. 8b). However, all impacts into rubble-pile target produce a shallower slope for fragments smaller than ~25 km. Since Eunomia is a rather old asteroid family, expected to have undergone significant collisional erosion especially among the smaller members of the family, would be difficult to start off with a SFD that is already deficient in numbers of smaller objects than is presently observed in the family.

4.2. Hygiea family

This family, with one of the largest and most massive bodies in the outer belt, has about 781 members. Carruba (2013) carried out a complete study of the orbital region of the Hygiea family in order to obtain good estimates of the family membership, asteroid halo extensions, cumulative SFD, etc. He claims that an interesting and unresolved problem is to explain how (10) Hygiea itself has an inclination slightly smaller than that of the rest of the family. Subsequently, they propose the Hygiea family was most probably formed by a cratering event and, depending of the geometry of the impact, the fragments were ejected into orbits with slightly higher angular momentum.

Fig. 8 (bottom panels) shows the best matches to the Hygiea family for $D = 400$ km monolithic and rubble-pile targets. We identified three impact events from a rubble-pile target that produce SFDs quite similar to the one observed for the Hygiea family (Fig. 8d). The best match corresponds to a projectile of $D = 54.4$ km im-

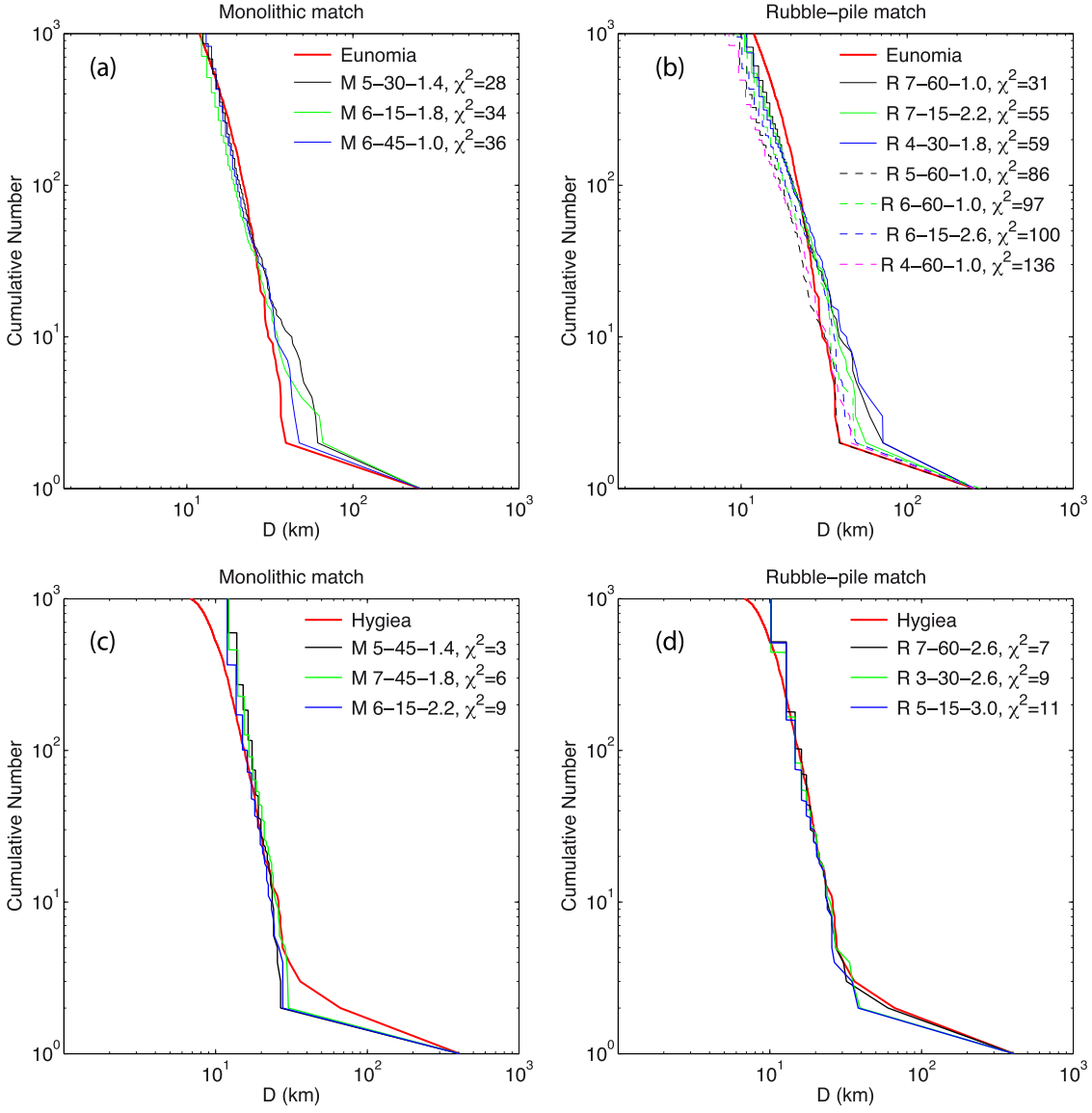

Fig. 8. Best matches to the observed Eunomia (upper panels) and Hygiea (bottom panels) families from $D = 400$ km monolithic and rubble-pile targets. Each plot shows the overall SFD of the family (solid red line) and the shifted modeled ones. The modeled curves are labeled as follows: internal structure of the target, impact speed, impact angle, and $\log(M_T/m_p)$, separated by dashes (e.g., Monolithic 6–45–1.0 means 6 km s^{-1}, 45°, and 1.0). The χ^2 is indicated for each case. (For interpretation of the references to colour in this figure legend, the reader is referred to the web version of this article.)

pacting at a speed of 7 km/s and a 60° impact angle. The next two best matches have a little less impact energy (corresponding to the cases R 3-30-2.6 and R 5-15-3.0), both leave a second largest fragment slightly smaller than the observed one. The three impacts produce cratering events where the largest fragment, (10) Hygiea, would retain 94% of the parent body. Then, the estimated parent body diameter is ~416 km, slightly smaller than that estimated through geometrical models. The fact that our best-matching SFD corresponds to a cratering event and not to a significant disruptive event could support the hypothesis of Carruba (2013) to explain the inclination of (10) Hygiea.

For completeness, Fig. 8c shows the "best" monolithic matches. All of these modeled SFDs share the same feature: they match quite well the observed SFD for smaller fragments ($D < 20$ km), however, none of them match the range from intermediate size (from ~20 km) to the second-largest fragment.

4.3. Vesta family

This is a cratering family located in the inner asteroid belt. Previous age estimation from Broz et al. (2013) gives 1000 ± 250 Myr in agreement with Spoto et al. (2015). It is widely accepted that 4 Vesta has a differentiated structure, recently confirmed by the spectroscopic measurements of the Dawn mission (De Sanctis et al. 2012).

Fig. 9 (upper panels) shows the best matches to the Vesta family for $D = 400$ km monolithic and rubble-pile targets. We propose five different impact conditions from a monolithic target (Fig. 9a). It is worth noting that the case M 6-75-1.8 leaves the second larger fragment quite similar to the observed one, being much smaller in other cases. This last objection can also be applied to rubble-pile targets, which best matches are shown in Fig. 9b.

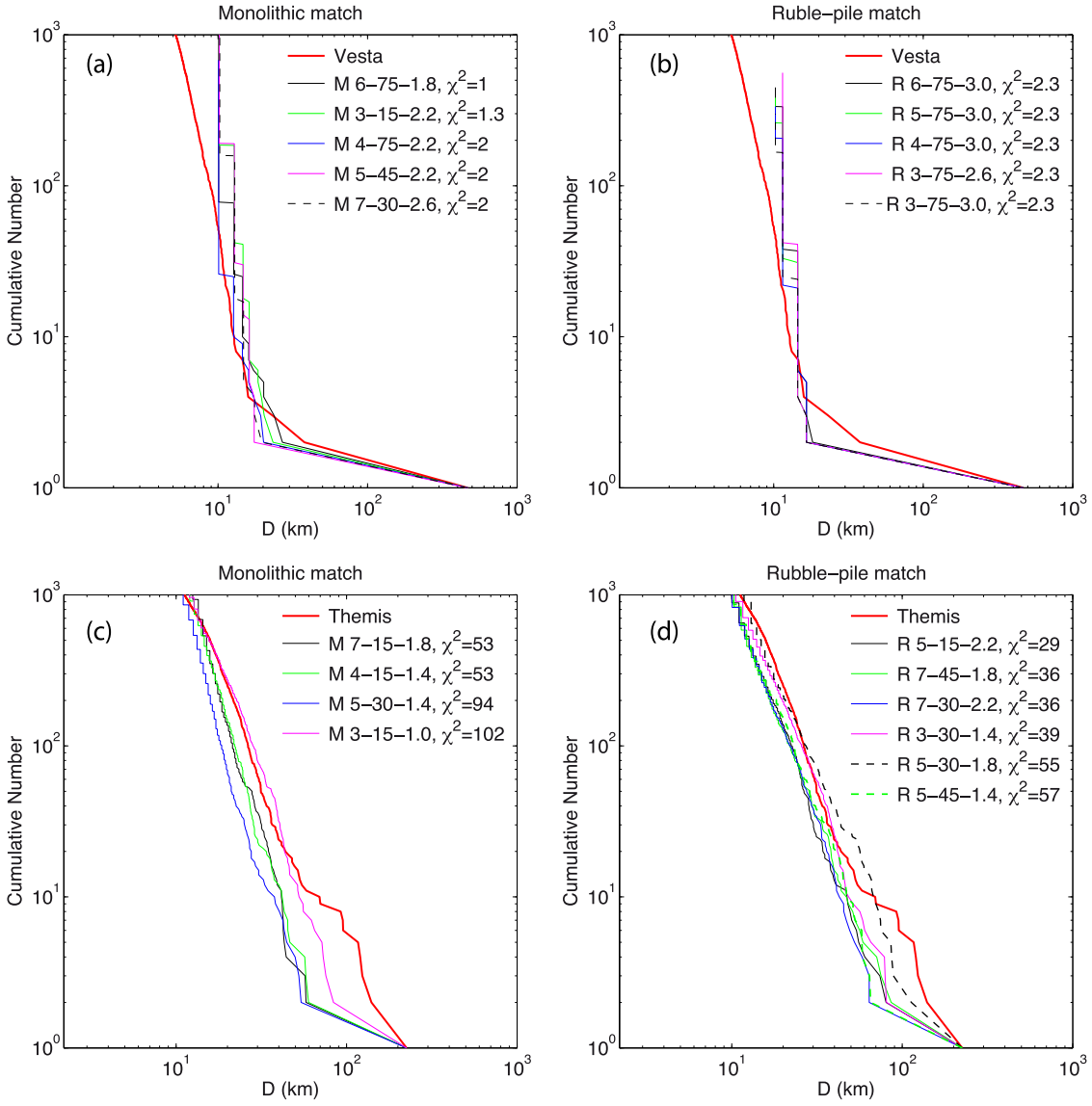

Fig. 9. Best matches to the observed Vesta (upper panels) and Themis (bottom panels) families from $D = 400$ km monolithic and rubble-pile targets. Each plot shows the overall SFD of the family (solid red line) and the shifted modeled ones. The modeled curves are labeled as follows: internal structure of the target, impact speed, impact angle, and $\log(M_T/m_p)$, separated by dashes (e.g., Monolithic 6–45–1.0 means 6 km s^{-1}, 45°, and 1.0). The χ^2 is indicated for each case. (For interpretation of the references to colour in this figure legend, the reader is referred to the web version of this article.)

4.4. Themis family

This is a large family with more than 5000 members (Nesvorný, 2012) located in the outer asteroid belt. Previous age estimation from Broz et al. (2013) gives $\sim 2.5 \pm 1.0$ Gyr in agreement with Spoto et al. (2015). The Themis family is very intriguing due to the diverse information that we know about its members. As Marsset et al. (2016) sum up, a) some members classified as main-belt comets have been identified in this family; b) water has been detected on the surface of (24) Themis; and c) at least two binary systems have been observed in this family: (90) Antiope and (379) Huenna, both with quite low primary densities < 1.3 g/cm^3. It is also worth mentioning that a young (< 10 Myr) subfamily (656) Beagle has been identified in the Themis family (Nesvorný et al., 2008).

Fig. 9 (bottom panels) shows the best matches to the Themis family for $D = 400$ km monolithic and rubble-pile targets. For both types of target we found some potential cases that match fairly well the slope of the SFD for fragments with $D < 60$ km. However, this family has a bump in the SFD around 60 to 110 km that is not well reproduced by any simulation performed in this work.

5. Discussion and conclusions

In this paper we have analyzed, in a systematic way, the broad features resulting from impacts onto both rubble-pile and monolithic parent bodies of $D = 100$ km and $D = 400$ km. We have also used the impact outcomes to attempt to constrain the impact conditions at the origin of known asteroid families with a large expected parent body.

From the present study the following conclusions may be obtained:

- The relative mass of the largest remnant is larger in the case of D= 400 km targets compared to D= 100 km targets. We have also observed a slight tendency to larger ratios D_1/D_2 in the case of 400 km targets, which corresponds to the “hockey stick” SFD morphology, common in cratering events. However the features in the SFD are not easily scalable from a 100 km tar-

get to a 400 km one. The only exceptions are the most super-catastrophic impacts into rubble-pile targets at impact angles ≤ 45°, which give a rather convex shape to the SFD (in the sense of Durda et al., 2007).

- The SFD slope shows a dependence on the impact specific energy. The slope tends to become shallower for increasing impact energy in the cratering regime. No significant speed dependence is observed, but from the projectile size alone it seems there may be some sort of strain-rate-dependent effect. An interpretation for this could be that smaller projectiles produce a sharp stress pulse on the target and activate small flaws, making small fragments. Conversely, when the impact reaches the critical fragmentation energy, the SFD slope becomes steeper as the impact energy increases.
- A dependence of M_2/M_T on the specific impact energy was also observed. It has a positive slope in the cratering regime and turns to negative slope for fragmentation events, so M_2 decreases as the impact energy increases.
- We have analyzed the main features seen in the cumulative SFD and on this basis we can say that the main conclusion from Benavidez et al. (2012) is still valid for 400 km targets. Namely, low-energy impacts into rubble-pile and monolithic targets produce such different features in the resulting SDF that they could be suitable for diagnosing the impact conditions and the internal structure of the parent body of the family.
- Building on our SFD comparison of $\underline{D} = 100$ and $\underline{D} = 400$ km targets, the effects of gravitational reaccumulation among fragments from small or large parent bodies do not produce directly scalable results. Hence, we uphold the caveat mentioned in previous studies (Durda et al., 2007 and Benavidez et al., 2012) that one might expect that the results of actual simulations involving significantly larger or smaller parent bodies might vary from the scaled results presented here because of enhanced or decreased gravitational effects among the debris in larger- or smaller-scale impacts. However, thanks to the extra simulation performed with 350 and 450 km diameter, we tested that it should be safe to use the shift method when the simulated and the real parent body are not more different in diameter than about 100 km. Under this circumstance, we observed that the uncertainties are lower (< 5.5%) for low and moderate impact energy. Whereas for high impact (super-catastrophic) events the uncertainties could increase up to ∼ 17%.
- We attempted to find the best match between the modeled and observed SFDs for the following asteroid families: Hygiea, Eunomia, Vesta and Themis. For the Hygiea family, a good match was found that corresponds to a cratering event onto a rubble-pile target involving a projectile of 54.4 km at 7 km/s and impact angle of 60°. Regarding the monolithic target, all the "best" potential cases have problems fitting the size range from ∼25 to ∼70 km. The fact that a rubble-pile target gives the best match may be an unexpected result. However, the match is highly convincing and can motivate further studies considering rubble-pile internal structures in the asteroid belt.

  For the Eunomia and Vesta families we found fairly good matches. For Eunomia, the best match corresponds to a super-catastrophic breakup onto a monolithic target that was impacted by a projectile of ∼186 km at 6 km/s and impact angle of 45°. Regarding impact simulations with a rubble-pile target, we found at least four different impact conditions that match the observed SFD for fragments larger than ∼25 km. However, below this size, the modeled SFD slope became shallower than the observed one. We rule out these cases on this basis. On the other hand, Milani et al., (2014) found two subfamilies within Eunomia, which they attribute to separate cratering events. This could suggest that some collisional process have happened in this family, modifying its SFD at some level. Then, this could explain why the matches found are fairly acceptable but not perfect. It should be studied carefully in further works.

  For the Vesta family, an impact simulation with a monolithic target impacted by a projectile of ∼100 km at 6 km/s and impact angle of 75° is the one that best matches the observed SFD. The agreement is quite good for fragments of $\underline{D} > 15$ km, but below this size the modeled SFD slope remains very steep as is usual for such oblique impacts. The parent body size estimated from this impact is of $\underline{D} = 468$ km, in good agreement with the geometrical estimation. It could be interesting to explore the breakup of monolithic target of D ∼ 500 km to achieve stronger conclusions for this family.

  Finally, for the Themis family it was not possible to find a good match. From either monolithic or rubble-pile targets it is possible to match the largest fragment and the SFD slope for $\underline{D} < 60$ km, however it is hard to reproduce the observed bump around 100 km. The $\chi 2$ value suggests that the SFDs of rubble-pile cases (compare Figs. 9c and d) are closer to the observed one, but there are no really satisfactory matches because the bump is not as bulging as in the Themis SFD. The fact we could not find an acceptable match for this family could be due to several reasons: a) the modeled internal structures in this work are very simple and the Themis family could have a more complex internal structure. In this sense, Castillo-Rogez and Schmidt (2010), motivated by the detection of water at the surface of 24 Themis (Rivkin and Emery, 2010; Campins et al., 2010), examined the possibility of the Themis parent body being a differentiated body made of a mixture of ice and rock. More recently, Marsset et al. (2016), based on the compositional characterization of some Themis family members, provide results supporting this hypothesis. b) The existence of the Beagle subfamily indicates that the Themis family has undergone some collisional activity over time. Such collisions could have modified the SFD produced by the original breakup that formed the Themis family. c) It could be possible that the Themis parent body had a size around 250 – 300 km or different bulk density than the simulated targets. Themis is a family dominated by primitive asteroids of C- and B-type; the estimated density for such asteroid types is about 2 g/cm3 (Baer & Chesley 2008), while the densities used in this study are 1.835 g/cm3 and 2.7 g/cm3 for rubble-pile and monolithic targets respectively. One might expect that more dense targets (with the same internal structure) are harder to break up given that the critical impact specific energy increases with bulk density, leading to some differences in the resulting SFD. It could be advisable to perform a new suite of simulations using the latest understanding of the physical features of Themis to achieve more accurate conclusions on this intriguing family.

- Finally, we conclude that an extension of impact simulation models to differentiated targets is necessary to build a more complete picture of the impact physics.

Acknowledgments

This work was partly supported by the Spanish Ministerio de Ciencia e Innovacion (now expired) grant AYA2011-30106-C02-02.

Appendix A

Modeled SFDs for monolithic and rubble-pile targets of D= 100 km and 400 km.

.

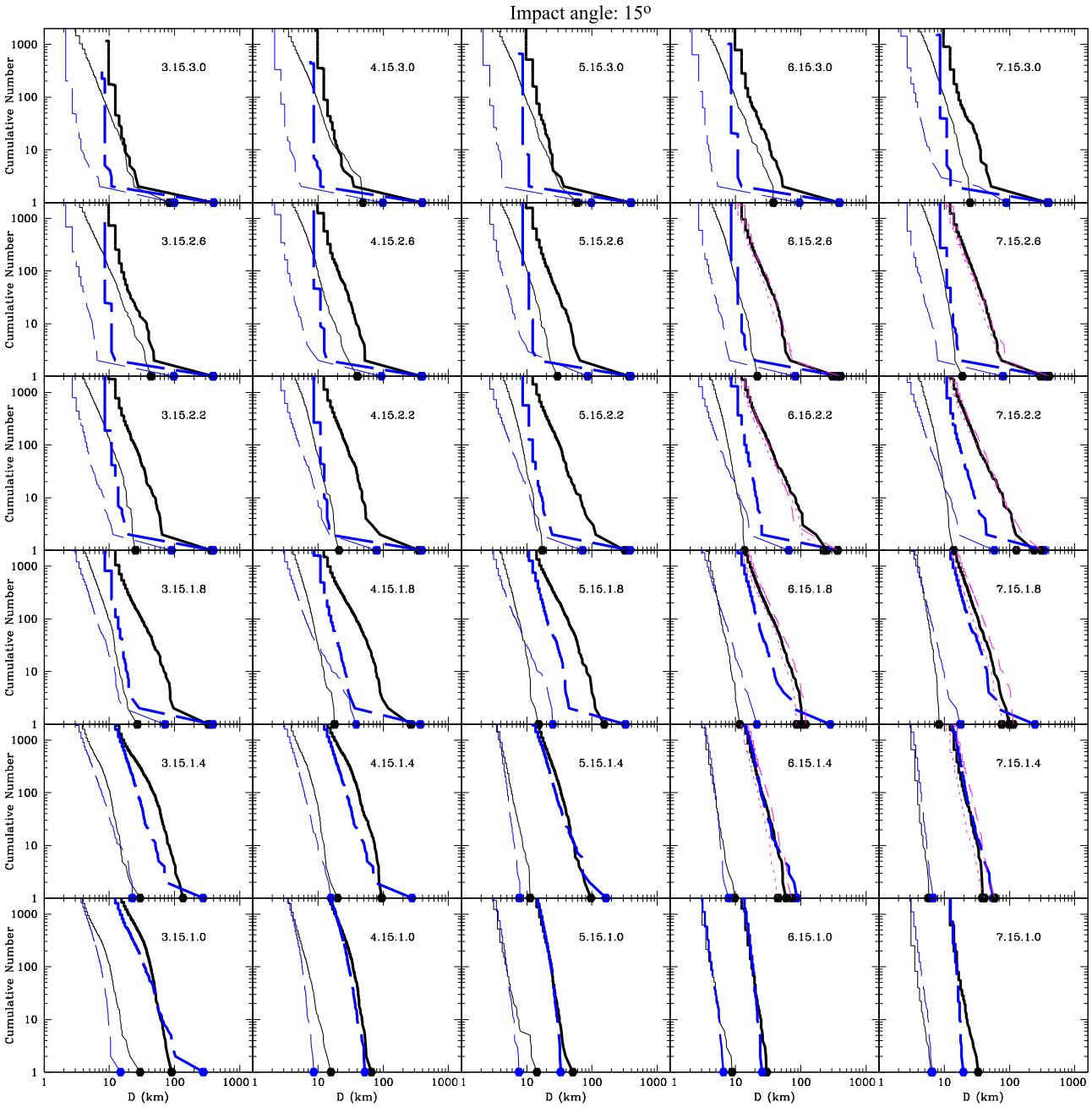

Fig. A.1. Modeled size-frequency distributions for rubble-pile (solid black line) and monolithic (dashed blue line) targets. The labels in each box indicate impact conditions as impact speed-impact angle-log(M_T/m_p). In all cases the thin line corresponds to the $D = 100$ km target and the thick one to $D = 400$ km. Some extra simulations were performed for $D = 350$ and D 450 km targets; these are drawn with short- and long-dashed lines, respectively, thin and pink.) (For interpretation of the references to colour in this figure legend, the reader is referred to the web version of this article.)

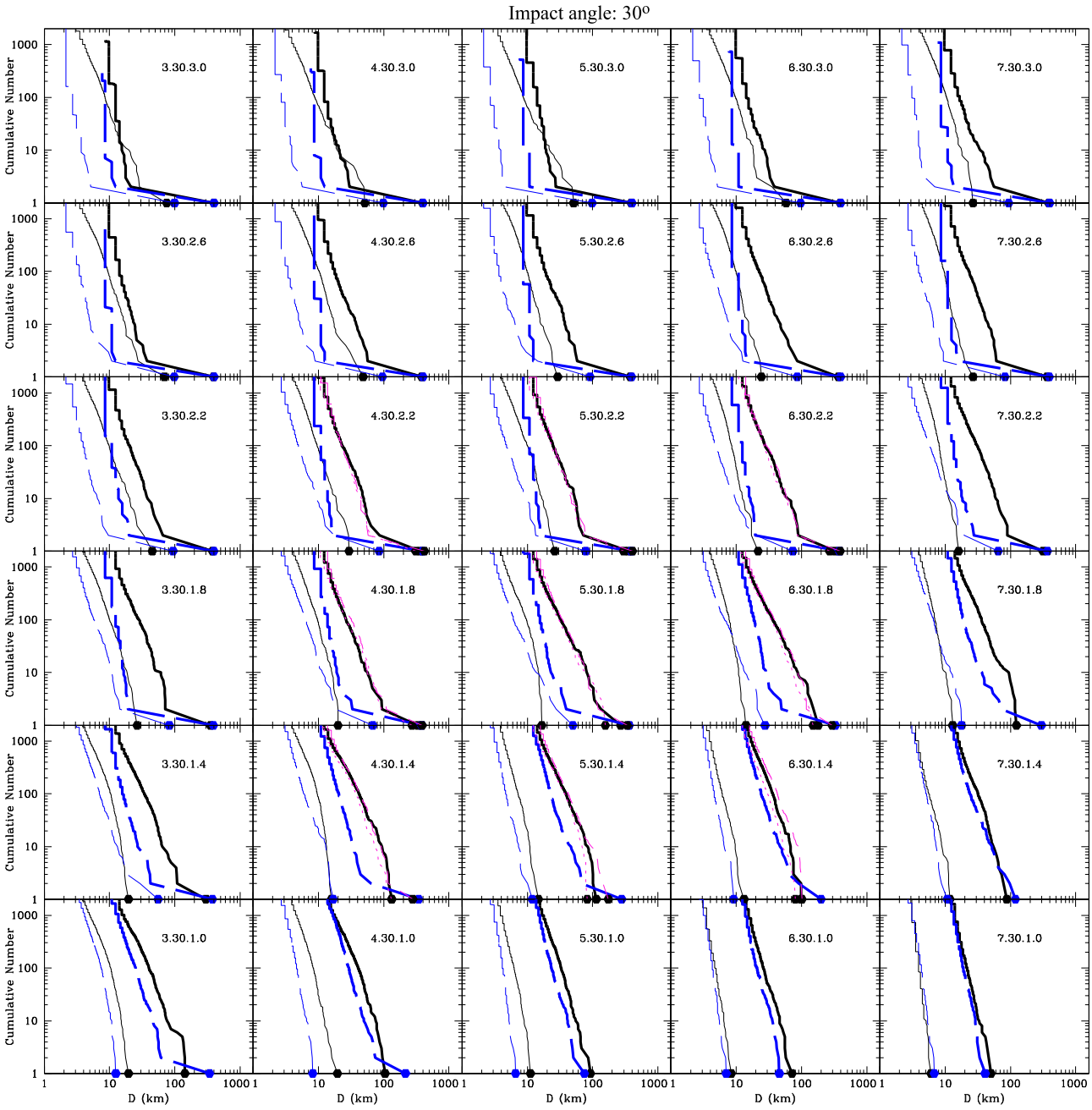

Fig. A.1.. (Continued)

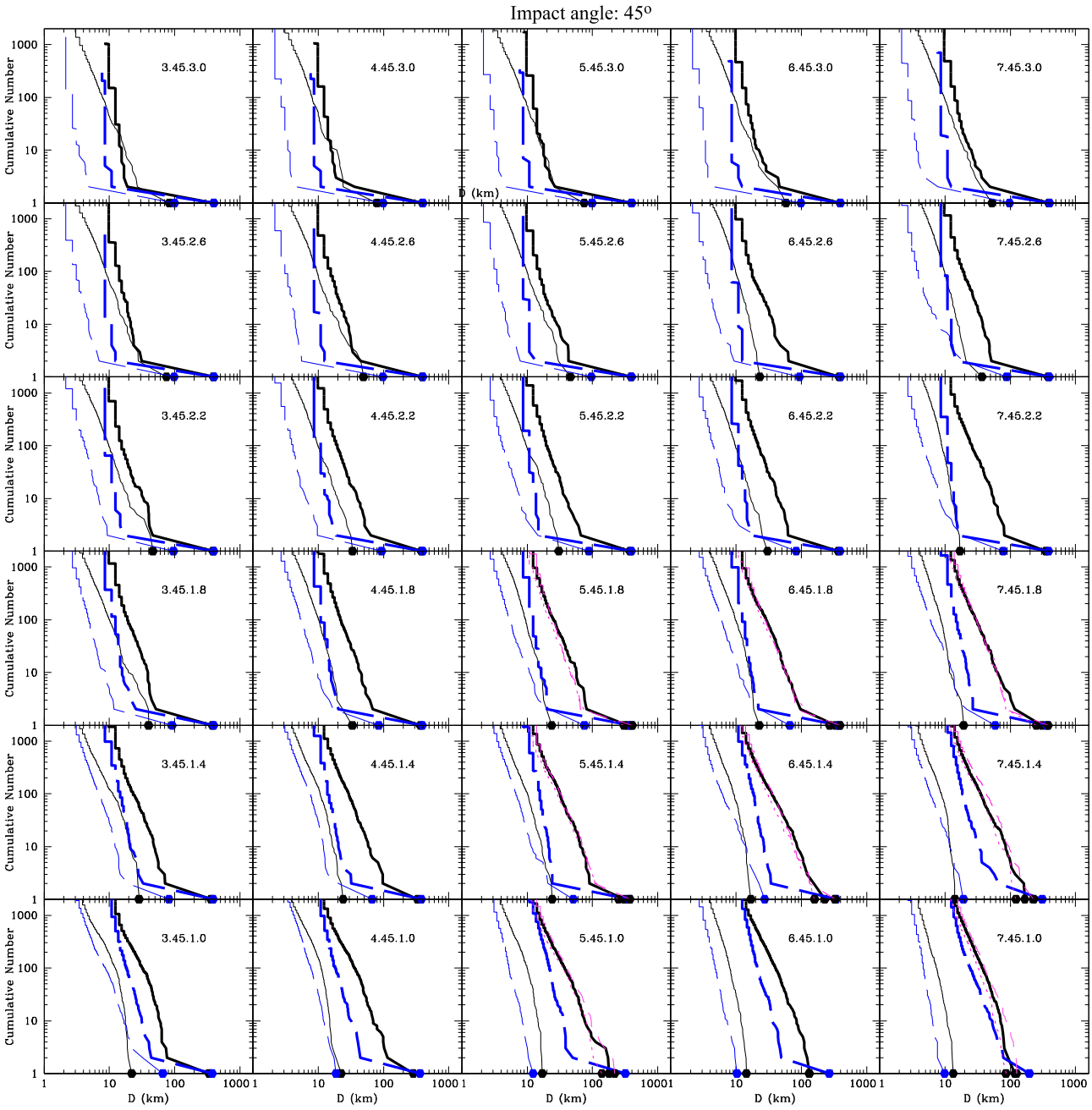

Fig. A.1. (Continued)

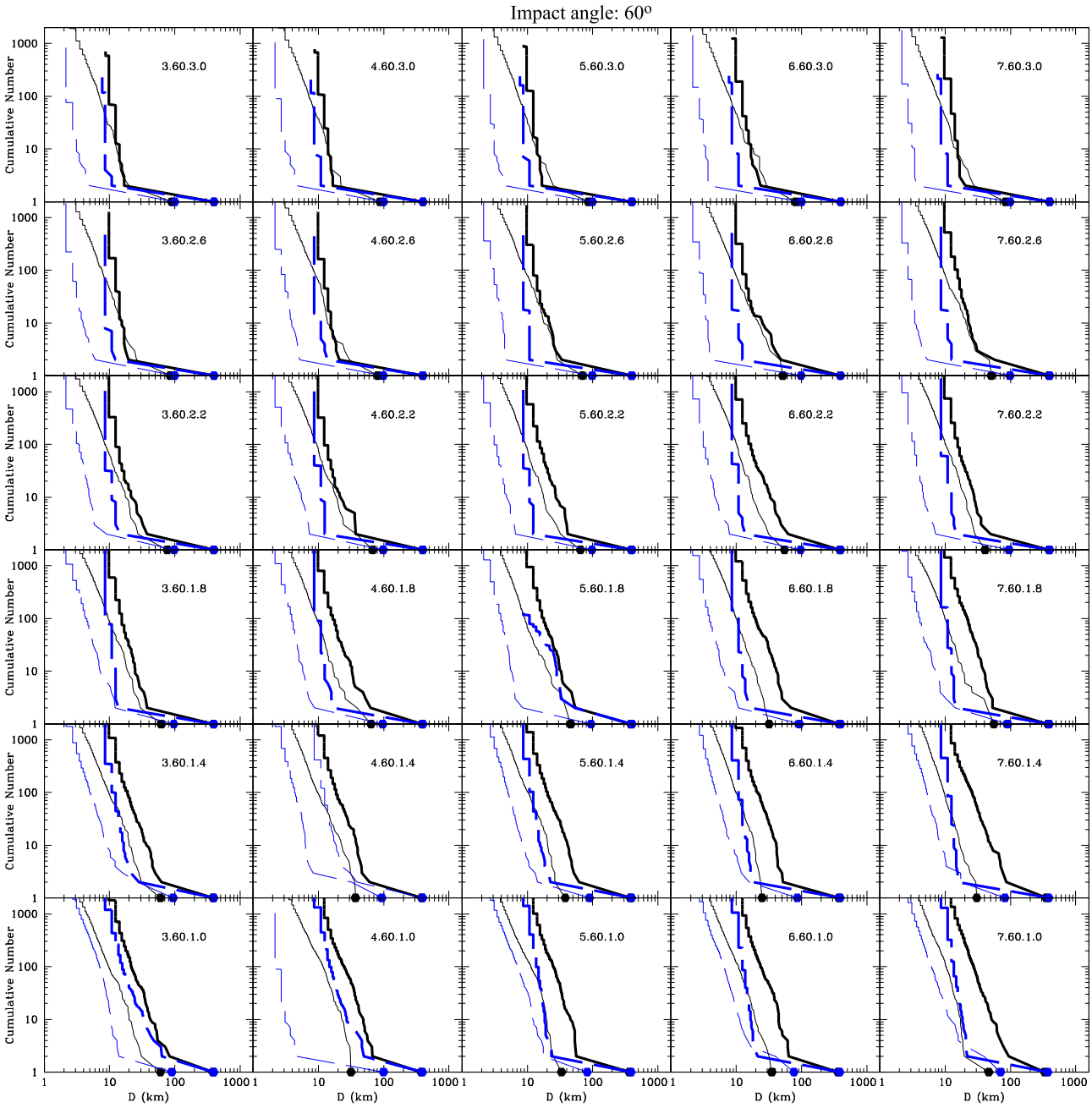

Fig. A.1. (Continued)

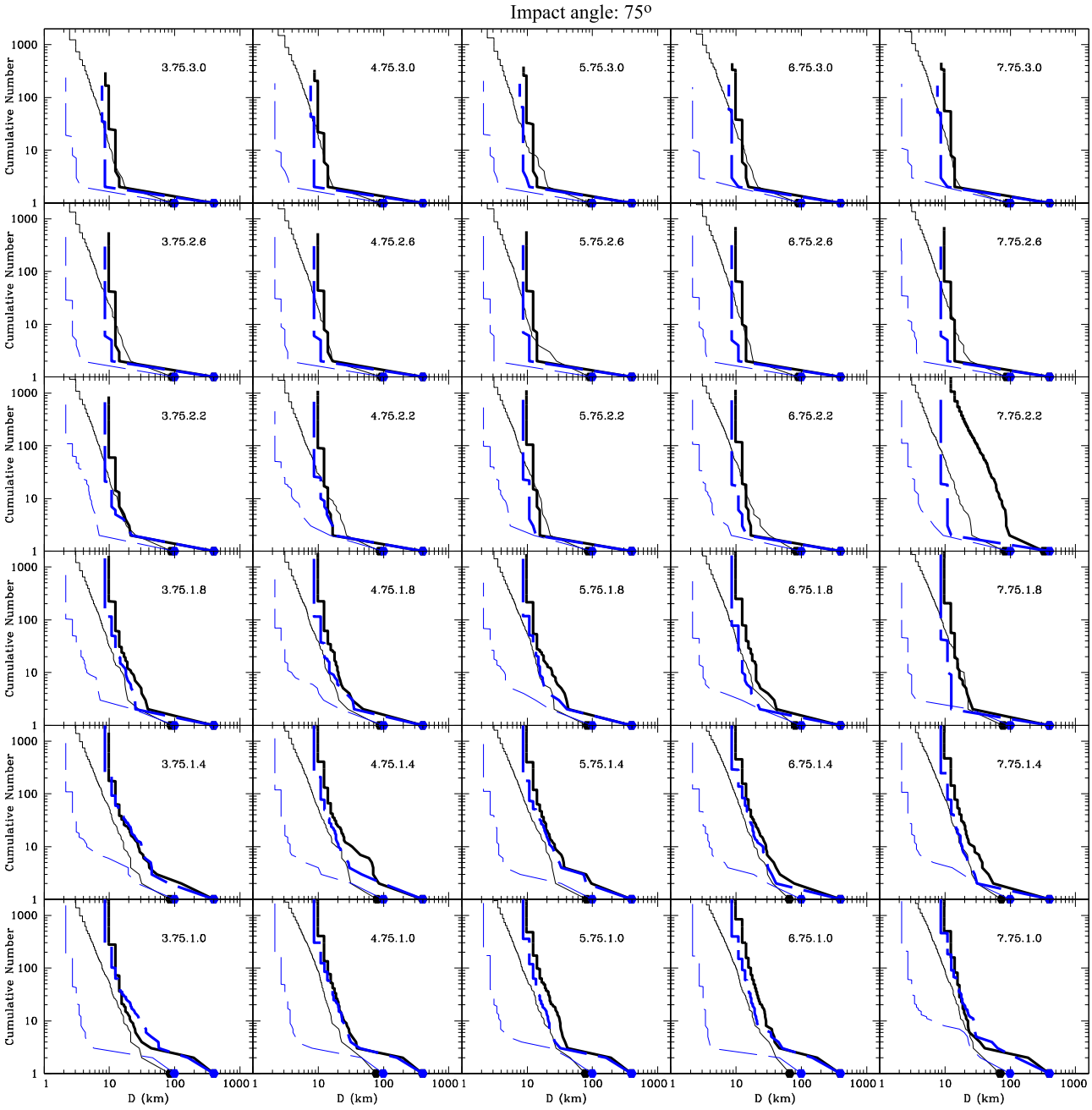

Fig. A.1. (Continued)

References

Arakawa, M., 1999. Collisional disruption of ice by high-velocity impact. Icarus 142, 34.

Asphaug, E., Melosh, H.J., 1993. The stickney impact of PHOBOS - a dynamical model. Icarus 101, 144.

Asphaug, E., Ryan, E.V., Zuber, M.T., 2002. Asteroid interiors. In: Bottke, W.F., Cellino, A., Paolicchi, P., Binzel, R.P. (Eds.), Asteroids III. Univ. of ArizonaPress, Tucson, pp. 463–484.

Asphaug, E., Collins, G., Jutzi, M., 2015. Global Scale Impacts. In: Michel, Patrick, DeMeo, Francesca E., Bottke, Jr., William F. (Eds.), Asteroids IV. University of Arizona Press, pp. 661–677.

Baer, J., Chesley, S.R., 2008. Astrometric masses of 21 asteroids, and an integrated asteroid ephemeris. Celestial Mech. Dyn. Astron. 100, 27.

Benavidez, P.G., Durda, D.D., Enke, B.L., et al., 2012. A comparison between rubble-pile and monolithic targets in impact simulations: Application to asteroid satellites and family size distributions. Icarus 219, 57.

Benz, W., Asphaug, E., 1994. Impact simulations with fracture. I - method and tests. Icarus 107, 98.

Benz, W., Asphaug, E., 1995. Simulations of brittle solids using smooth particle hydrodynamics. Comput. Phys. Commun. 87, 253.

Benz, W., Asphaug, E., 1999. Catastrophic disruptions revisited. Icarus 142, 5.

Bottke, W.F., Durda, D.D., Nesvorný, D., et al., 2005. The fossilized size distribution of the main asteroid belt. Icarus 175, 111.

Broz, M., Morbidelli, A., Bottke, W.~F., et al., 2013. Constraining the cometary flux through the asteroid belt during the late heavy bombardment. Astron. Astrophys. 551, A117.

Campo Bagatin, A., Petit, J.-M., Farinella, P., 2001. How many rubble-piles are in the asteroid belt? Icarus 149, 198.

Campo Bagatin, A., Petit, J.-M., 2001. Effects of the geometric constraints on the size distributions of debris in asteroidal fragmentation. Icarus 149, 210.

Campins, H., Hargrove, K., Pinilla-Alonso, N., et al., 2010. Water ice and organics on the surface of the asteroid 24 Themis. Nature 464, 1320.

Carruba, V., 2013. An analysis of the Hygiea asteroid family orbital region. MNRAS 431, 3557.

Castillo-Rogez, JulieC., Schmidt, B.E., 2010. Geophysical evolution of the Themis family parent body. Geophys. Res. Lett. 37 (10) CiteID L10202.

Cibulková, H., Bro˘z, M., Benavidez, P.G., 2014. A six-part collisional model of the main asteroid belt. Icarus 241, 358.

De Sanctis, M.C., Combe, J.-P., Ammannito, E., et al., 2012. Detection of wide spread hydrated materials on vesta by the vir imaging spectrometer on board the dawn mission. ApJ 758, L36.

Dell'Oro, A., Paolicchi, P., 1998. Statistical properties of encounters among asteroids: a new, general, purpose, formalism. Icarus 136, 328–339.

Durda, D.D., Bottke, W.F., Enke, B.L., Merline, W.J., Asphaug, E., Richardson, D.C., Leinhardt, Z.M., 2004. The formation of asteroid satellites in large impacts: results from numerical simulations. Icarus 167, 382–396.

Durda, D.D., Bottke, W.F., Nesvorný, D., Enke, B.L., Merline, W.J., Asphaug, E., Richardson, D.C., 2007. Size frequency distributions of fragments from SPH/N-body simulations of asteroid impacts: Comparison with observed asteroid families. Icarus 186, 498–516.

Durham, W.B., McKinnon, W.B., Stern, L.A., 2005. Cold compaction of water ice, Geophys. Geophys. Res. Lett. 32, L18202. doi:10.1029/2005GL023484.

Fujiwara, A., Kamimoto, G., Tsukamoto, A., 1977. Destruction of basaltic bodies by high-velocity impact. Icarus 31, 277.

Jutzi, M., Michel, P., Benz, W., Richardson, D.C., 2010. Fragment properties at the catastrophic disruption threshold: the effect of the parent bodys internal structure. Icarus 207, 54–65.

Jutzi, Martin, Holsapple, K.A., Wünneman, K., Michel, P., 2015. Modeling asteroid collisions and impact processes. In: Michel, Patrick, DeMeo, Francesca, Bottke, Jr., E., William, F. (Eds.), Asteroids IV. University of Arizona Press, pp. 679–699.

Leinhardt, Z.M., Richardson, D.C., Quinn, T., 2000. Direct N-body simulations of rubble pile collisions. Icarus 146, 133–151.

Leinhardt, Z.M., Richardson, D.C., 2002. N-body simulations of planetesimal evolution: effect of varying impactor mass ratio. Icarus 159, 306–313.

Leinhardt, Z.M., Stewart, S.T., 2012. Collisions between gravity-dominated bodies. I. outcome regimes and scaling laws. ApJ 745, 79.

Leliwa-Kopystynski, J., Arakawa, M., 2014. Impacts experiments onto heterogeneous targets simulating impact breccia: implications for impact strength of asteroids and formation of the asteroid families. Icarus 235, 147.

Marsset, M., Vernazza, P., Birlan, M., et al., 2016. Compositional characterisation of the Themis family. Astron. Astrophys. 586, A15.

Michel, P., Benz, W., Tanga, P., Richardson, D.C., 2001. Collisions and gravitational reaccumulation: forming asteroid families and satellites. Science 294, 1696–1700.

Michel, P., Tanga, P., Benz, W., Richardson, D.C., 2002. Formation of asteroid families by catastrophic disruption: simulations with fragmentation and gravitational reaccumulation. Icarus 160, 10–23.

Michel, P., Benz, W., Richardson, D.C., 2003. Disruption of fragmented parent bodies as the origin of asteroid families. Nature 421, 608–611.

Michel, P., Benz, W., Richardson, D.C., 2004. Catastrophic disruption of pre-shattered parent bodies. Icarus 168, 420–432.

Milani, A., Cellino, A., Knežević, Z., Novaković, B., Spoto, F., Paolicchi, P., 2014. Asteroid families classification: exploiting very large datasets. Icarus 239, 46.

Mothé-Diniz, T., Roig, F., Carvano, J.M., 2005. Reanalysis of asteroid families structure through visible spectroscopy. Icarus 174, 54.

Nesvorný, D., 2012. HCM asteroid families v2.0. EAR-a-VARGBDET-5 NESVORNYFAM-v2.0. NASA Planetary Data System.

Nesvorný, Bottke, Vokrouhlicky, et al., 2008. Origin of the near-ecliptic circumsolar dust band. Astrophys. J. 679, L143–L146.

Nesvorný, D., Jedicke, R., Whiteley, R.J., Ivezić, Ž., 2005. Evidence for asteroid space weathering from the Sloan Digital Sky Survey. Icarus 173, 132–152.

Nesvorný, D., Enke, B.L., Bottke, W.F., et al., 2006. Karin cluster formation by asteroid impact. Icarus 183, 296–311.

Pierazzo, E., Melosh, H.J., 2000. Understanding oblique impacts from experiments, observations, and modeling. Annu. Rev. Earth Planet. Sci. 28, 141.

Richardson, D.C., Quinn, T., Stadel, J., Lake, G., 2000. Direct large-scale N-body simulations of planetesimal dynamics. Icarus 143, 45–59.

Rivkin, A.S., Emery, J.P., 2010. Detection of ice and organics on an asteroidal surface. Nature 464, 1322.

Stadel, J.G., 2001. Cosmological N-body simulations and their analysis, Ph.D. Thesis. University of Washington, Seattle, p. 126.

Spoto, F., Milani, A., Knezevic, Z., 2015. Asteroid family ages. Icarus 257, 275.

Tanga, P., Cellino, A., Michel, P., Zappalà, V., Paolicchi, P., dell'Oro, A., 1999. On the size distribution of asteroid families: the role of geometry. Icarus 141, 65–78.

Tillotson, J.H., 1962. Metallic equations of state for hypervelocity impact. General Atomic Report GA-3216.